The Astrophysical Journal, 841:97 (14pp), 2017 June 1 https://doi.org/10.3847/1538-4357/aa6ff8
© 2017. The American Astronomical Society. All rights reserved.

A Massive Prestellar Clump Hosting No High-mass Cores

Patricio Sanhueza[1], James M. Jackson[2], Qizhou Zhang[3], Andrés E. Guzmán[4], Xing Lu[1], Ian W. Stephens[3], Ke Wang[5], and Ken'ichi Tatematsu[1]
[1] National Astronomical Observatory of Japan, National Institutes of Natural Sciences, 2-21-1 Osawa, Mitaka, Tokyo 181-8588, Japan
patricio.sanhueza@nao.ac.jp
[2] School of Mathematical and Physical Sciences, University of Newcastle, University Drive, Callaghan, NSW 2308, Australia
[3] Harvard-Smithsonian Center for Astrophysics, 60 Garden Street, Cambridge, MA 02138, USA
[4] Departamento de Astronomía, Universidad de Chile, Camino el Observatorio 1515, Las Condes, Santiago, Chile
[5] European Southern Observatory (ESO) Headquarters, Karl-Schwarzschild-Str. 2, D-85748 Garching bei München, Germany
Received 2017 February 24; revised 2017 April 23; accepted 2017 April 25; published 2017 May 30

Abstract

The infrared dark cloud (IRDC) G028.23-00.19 hosts a massive (1500 $M_\odot$), cold (12 K), and 3.6–70 μm IR dark clump (MM1) that has the potential to form high-mass stars. We observed this prestellar clump candidate with the Submillimeter Array (∼3.″5 resolution) and Jansky Very Large Array (∼2.″1 resolution) in order to characterize the early stages of high-mass star formation and to constrain theoretical models. Dust emission at 1.3 mm wavelength reveals five cores with masses $\leqslant$15 $M_\odot$. None of the cores currently have the mass reservoir to form a high-mass star in the prestellar phase. If the MM1 clump will ultimately form high-mass stars, its embedded cores must gather a significant amount of additional mass over time. No molecular outflows are detected in the CO (2-1) and SiO (5-4) transitions, suggesting that the SMA cores are starless. By using the NH_3 (1, 1) line, the velocity dispersion of the gas is determined to be transonic or mildly supersonic ($\Delta V_{\rm nt}/\Delta V_{\rm th} \sim$ 1.1–1.8). The cores are not highly supersonic as some theories of high-mass star formation predict. The embedded cores are four to seven times more massive than the clump thermal Jeans mass and the most massive core (SMA1) is nine times less massive than the clump turbulent Jeans mass. These values indicate that neither thermal pressure nor turbulent pressure dominates the fragmentation of MM1. The low virial parameters of the cores (0.1–0.5) suggest that they are not in virial equilibrium, unless strong magnetic fields of ∼1–2 mG are present. We discuss high-mass star formation scenarios in a context based on IRDC G028.23-00.19, a study case believed to represent the initial fragmentation of molecular clouds that will form high-mass stars.

Key words: ISM: clouds – ISM: individual objects (IRDC G028.23-00.19) – ISM: kinematics and dynamics – ISM: molecules – stars: formation

1. Introduction

For many decades, the study of high-mass star formation has been biased toward the more evolved, brighter, and more easily detected protostellar phases. In recent years, the study of the elusive prestellar phase, before the existence of embedded heating sources, has been recognized as key in constraining models of high-mass star formation (e.g., Zhang et al. 2009; Pillai et al. 2011; Wang et al. 2011; Tan et al. 2013). However, due to the small known sample of prestellar sources that have the potential to form high-mass stars (>8 $M_\odot$), the current observational evidence is inconclusive and sometimes supports or refutes the same theoretical predictions.

Seen as dark silhouettes against the Galactic mid-infrared background in Galactic plane surveys (*ISO*; Perault et al. 1996; *MSX*, Egan et al. 1998; Simon et al. 2006; *Spitzer*, Peretto & Fuller 2009; Kim et al. 2010), infrared dark clouds (IRDCs) are believed to host the earliest stages of star formation. Several studies have investigated the kinematic and filamentary structure of IRDCs (Foster et al. 2014; Henshaw et al. 2014; Liu et al. 2014; Dirienzo et al. 2015; Ragan et al. 2015; Contreras et al. 2016; Henshaw et al. 2016), as well as their chemistry (Sakai et al. 2008, 2012, 2015; Sanhueza et al. 2012, 2013; Hoq et al. 2013; Miettinen 2014; Vasyunina et al. 2014; Feng et al. 2016a; Kong et al. 2016). Evidence of active high-mass star formation in IRDC clumps[6] is inferred by the presence of ultracompact (UC) H II regions (Battersby et al. 2010; Avison et al. 2015), thermal ionized jets (Rosero et al. 2014, 2016), hot cores (Rathborne et al. 2008; Sakai et al. 2013), embedded 24 μm sources (Chambers et al. 2009), molecular outflows (Sanhueza et al. 2010; Wang et al. 2011, 2014; Lu et al. 2015), or maser emission (Pillai et al. 2006; Wang et al. 2006; Chambers et al. 2009; Yanagida et al. 2014). On the other hand, IRDC clumps with similar masses and densities that lack all the previously mentioned star formation indicators are the prime candidates to be in the prestellar phase. The prestellar phase still remains the least characterized and understood stage of the formation of high-mass stars.

Recently, several high-mass cluster-forming clumps that are candidates to be in the prestellar phase have been found mainly using *Herschel* observations (Guzmán et al. 2015; Traficante et al. 2015) in combination with line surveys (e.g., Foster et al. 2011; Jackson et al. 2013; Shirley et al. 2013; Rathborne et al. 2016). However, only a few targets have been followed up in detail to confirm the lack of star formation. A prestellar, high-mass cluster-forming clump completely devoid of active high-mass star formation (Sanhueza et al. 2013) and prestellar cores embedded in high-mass cluster-forming clumps (Pillai et al. 2011; Beuther et al. 2013; Tan et al. 2013; Cyganowski et al. 2014; Ohashi et al. 2016) stand out as the best candidates to study the prestellar phase in the high-mass star formation regime because they have been studied in depth using space-borne telescopes, single-dish ground-based radio telescopes, and radio interferometers. Prestellar core candidates that can form high-mass stars have

[6] Throughout this paper, we use the term "clump" to refer to a dense object within an IRDC with a size of the order of ∼0.2–1 pc, a mass of $\sim 10^2$–10^3 $M_\odot$, and a volume density of $\sim 10^4$–10^5 cm^{-3}. We use the term "core" to describe a compact, dense object within a clump with a size of ∼0.01–0.1 pc, a mass of ∼1–10^2 $M_\odot$, and a volume density $\gtrsim 10^5$ cm^{-3}.

been exclusively found only toward active high-mass cluster-forming clumps. The prestellar core masses have a few tens of solar masses with volume densities larger than $10^5\,\mathrm{cm}^{-3}$ (Pillai et al. 2011; Beuther et al. 2013; Tan et al. 2013; Cyganowski et al. 2014; Ohashi et al. 2016). In these cores, there is strong observational evidence that turbulence alone cannot provide sufficient support against gravity to avoid rapid collapse (virial parameters less than unity; Pillai et al. 2011; Tan et al. 2013; Lu et al. 2015; Zhang et al. 2015; Ohashi et al. 2016). Magnetic fields, which are known to play an important role in the formation of dense cores in more evolved massive clumps (Zhang et al. 2014), may also be important in clumps at earlier stages of evolution.

1.1. High-mass Star Formation Theories

Current theories of high-mass star formation can be primarily separated in the way that the stars acquire their mass from the environment: core accretion ("core-fed") and competitive accretion ("clump-fed"). The turbulent core accretion model (McKee & Tan 2003) posits that all stars form by a top-down fragmentation process in which a cluster-forming clump fragments into cores under the combined effects of self-gravity, turbulence, and magnetic fields. These cores are gravitationally bound, and they are the entities that directly feed the central protostars ("core-fed"). The pressure support that maintains the cores close to internal virial equilibrium is provided by turbulence and/or magnetic fields. Cores have no significant further accumulation of gas from the surrounding medium, implying that the final stellar mass is smaller than the core mass. The core mass is set at early times and, thus, in order to form a high-mass star, a high-mass core must exist in the prestellar phase. Therefore, the core accretion theory predicts a direct relationship between the distribution function of core masses, known as the core mass function (CMF), and the mass distribution function of newly formed stars, known as the the initial mass function (IMF; Tan et al. 2014). However, it is not clear what prevents a high-mass core from fragmenting into several low-mass cores. According to Krumholz & McKee (2008), the heat produced by accreting low-mass stars in regions with surface densities of at least $1\,\mathrm{g\,cm}^{-2}$ can halt fragmentation of the high-mass core. However, this mechanism to prevent fragmentation has been questioned by Zhang et al. (2009), Smith et al. (2009), Longmore et al. (2011), Wang et al. (2012), and Tan et al. (2013). Commerçon et al. (2011) and Myers et al. (2013) suggest that magnetic fields, combined with radiative feedback, can strongly suppress core fragmentation. However, direct observations of magnetic fields in very early stages of high-mass star formation remain difficult, although observations in regions with high-mass protostars appear to indicate that magnetic fields are important (Girart et al. 2009; Qiu et al. 2014; Zhang et al. 2014; Li et al. 2015).

Competitive accretion models posit that a cluster-forming clump fragments into cores with masses close to the thermal Jeans mass (Bonnell et al. 2004), $\sim 2\,M_\odot$ at a volume density and temperature of $5 \times 10^4\,\mathrm{cm}^{-3}$ and 12 K, respectively. None of these cores are massive enough to form a high-mass star. However, the cores that are located at the center of the clump's gravitational potential can accrete, via modified Bondi–Hoyle accretion, sufficient mass over time to grow and eventually form high-mass stars. One important distinction from the turbulent core accretion model is that the mass reservoir available to form the high-mass stars is accreted from material well beyond the original cores, and the gas is funneled down to the center of the clump due to the entire clump's gravitational potential by a large-scale infall ("clump-fed"). Thus, the core mass is gathered during the star formation process itself and is not set in the prestellar stage. The final stellar mass is therefore predicted to be larger than the initial core mass. According to competitive accretion, there are no high-mass prestellar cores, which is in disagreement with the turbulent core accretion model. A consequence of competitive accretion is that high-mass stars would be always formed near the center of stellar clusters. Krumholz et al. (2005) suggest that a subvirial state is required for competitive accretion to allow the formation of high-mass stars. However, Bonnell & Bate (2006) show that this is not the case for the simulations in Bonnell et al. (2003). On the other hand, in the simulations of Wang et al. (2010), the material near the vicinity of the newly formed stars is not supported by turbulence nor magnetic fields, and it is typically in a state of rapid collapse (subvirial).

1.2. IRDC G028.23-00.19

In this work, we aim to characterize the prestellar phase in the high-mass regime in order to test predictions of high-mass star formation theories. Sanhueza et al. (2013) studied a prestellar, high-mass cluster-forming clump candidate, MM1, located in the IRDC G028.23-00.19 ($\sim$5000 $M_\odot$) that has the potential to form high-mass stars. The whole IRDC has been recently observed in IR polarization, which allowed the determination of magnetic field strengths of 10–165 μG in the low-density regions at parsec scales (excluding MM1; Hoq et al. 2017). The massive clump MM1 is dark at *Spitzer*/IRAC 3.6, 4.5, and 8.0 μm (Benjamin et al. 2003), *Spitzer*/MIPS 24 μm (Carey et al. 2009), and *Herschel*/PACS 70 μm (Molinari et al. 2010). Remarkably, MM1 has a 24 μm optical depth ($\tau_{24\ \mu\mathrm{m}}$) close to unity, which is the highest in the IRDC sample studied by Dirienzo et al. (2015). The total mass of the clump is 1500 $M_\odot$, the radius $\sim$0.6 pc, the volume density $3 \times 10^4\,\mathrm{cm}^{-3}$, and its distance 5.1 kpc (Sanhueza et al. 2012, 2013). The clump is gravitationally unstable with a virial parameter significantly below unity ($\alpha = 0.3$). The spectral energy distribution from 250 μm to 1.2 mm and the rotational diagram of low excitation CH_3OH lines both reveal cold dust/gas emission of 12 K (Sanhueza et al. 2013). Observations at 1.3, 3.6, and 6 cm that searched for free–free emission (Battersby et al. 2010; Rosero et al. 2016) and H_2O and CH_3OH maser emission (Wang et al. 2006; Chambers et al. 2009) have resulted in null detections. The cold temperatures, coupled with the lack of several indicators of star formation, suggest that the massive clump MM1 is a pristine prestellar clump appropriate for the study of the earliest stages of high-mass star formation. By using high angular resolution observations from the Submillimeter Array[7] (SMA; $\sim 3\farcs5$ resolution) and Jansky Very Large Array (JVLA) ($\sim 2''$ resolution), we have searched for the embedded cores and determined their dynamical state at <0.1 pc scales.

[7] The Submillimeter Array is a joint project between the Smithsonian Astrophysical Observatory and the Academia Sinica Institute of Astronomy and Astrophysics, and is funded by the Smithsonian Institution and the Academia Sinica.

2. Observations

Observations of IRDC G028.23-00.19 were carried out with the SMA and the JVLA, operated by the National Radio Astronomy Observatory.[8]

2.1. SMA Observations

SMA 1.3 mm line and continuum observations were taken during 2012 April and 2013 July in the compact configuration. The projected baselines range from 10 to 69 m. The IRDC was completely mapped by combining images in a mosaic from five separate positions, using the same correlator setup that covers 4 GHz in each of the lower and upper sidebands. A spectral resolution of 1.1 km s^{-1} (0.812 MHz) was used. The continuum emission was produced by averaging the line-free channels in visibility space. Using natural weighting, the 1σ rms noise for the continuum emission is 0.75 mJy beam^{-1}.

The system temperature typically varied from 150 to 220 K during the observations. At the center frequency of 224.6975 GHz (1.3 mm), the primary beam or field of view of SMA is 56″. These SMA observations are sensitive to structure with angular scales smaller than ∼30″. The final synthesized beam has a size of 4.″1 × 3.″0 with a P.A. of −25°. The geometric mean of the major and minor axis is 3.″5, which corresponds to a physical size of ∼0.09 pc (∼18,000 au) at a distance of 5.1 kpc (Sanhueza et al. 2012).

The data from different tracks were calibrated separately using the IDL-based MIR package and exported to CASA to be combined in the visibility domain for imaging. Typical SMA observations may be subject to up to 15% of uncertainty in absolute flux scales. The quasar J1743-038 was periodically observed for phase calibration. The quasars J2202+422 (BL Lac) and J0319+415 (3C84) were used for bandpass calibration. Uranus and the bright radio continuum source MWC349A were used for flux calibration.

2.2. JVLA Observations

The JVLA observations consisted of two pointings at K-band (1.3 cm) covering the whole IRDC, taken in 2012 February in the C configuration. The projected baselines ranged from 50 to 3400 m. NH_3 (J, K) = (1, 1) at 23.6944955 GHz and NH_3 (J, K) = (2, 2) at 23.7226336 GHz were simultaneously observed with a spectral resolution of 0.4 km s^{-1} (31.25 kHz) in dual polarization mode. At these frequencies, the primary beam of JVLA is 1.′9. These observations are sensitive to angular scales smaller than ∼1′.

The data were calibrated and imaged using the CASA 4.2 software package. In order to improve the signal-to-noise ratio (S/N), a Gaussian filter "outertaper" of 1.″6 was applied during the CLEAN deconvolution, obtaining twice the original synthesized beam. Using natural weighting, the synthesized beam was 2.″3 × 2.″0 with a P.A. = 32° for both NH_3 lines, while the 1σ rms noise was 0.78 mJy beam^{-1} per channel for NH_3 (1, 1) and 0.75 mJy beam^{-1} per channel for NH_3 (2, 2). The conversion factor between mJy beam^{-1} to brightness temperature in K is 0.47 (1 mJy beam^{-1} = 0.47 K). The geometric mean of the major and minor axis is 2.″1, which corresponds to a physical size of ∼0.05 pc (∼11,000 au) at a distance of 5.1 kpc.

The bandpass and flux calibrations were performed by using observations of the quasar J1331+305 (3C286). The phase calibration was done by periodically observing the quasar J1851+0035.

[8] The National Radio Astronomy Observatory is a facility of the National Science Foundation operated under cooperative agreement by Associated Universities, Inc.

3. Will the Clump MM1 in IRDC G028.23-00.19 form High-mass Stars?

Current observational evidence supports the idea that the clump MM1 will form high-mass stars. In addition, the clump properties are also consistent with those used in simulations that produce stellar clusters including high-mass stars. We assess the potential to form high-mass stars of the IRDC G028.23-00.19 below.

(i) Based on the observed relation between the maximum stellar mass in a cluster ($m_{\rm max}$) and the total mass of the cluster ($M_{\rm cluster}$), given by (Larson 2003)

$$\left(\frac{m_{\rm max}}{M_\odot}\right) = 1.2\left(\frac{M_{\rm cluster}}{M_\odot}\right)^{0.45}, \quad (1)$$

the mass of the most massive star that will be formed in a cluster-forming clump can be estimated. Assuming a cluster star formation efficiency of 30% (Lada & Lada 2003; Alves et al. 2007), the clump MM1 in IRDC G028.23-00.19, which has a mass of 1500 $M_\odot$, should form a stellar cluster of a total mass of 450 $M_\odot$. According to the discussion in Section 5.6, the uncertainty in the mass is 50%. Larson's relationship then predicts that this clump will form one high-mass star of 19 ± 4 $M_\odot$. Even with only 5% star formation efficiency, a 8 ± 2 $M_\odot$ star should be formed.

Using the IMF from Kroupa (2001), the maximum stellar mass of a clump can also be estimated and is given by (see the Appendix)

$$m_{\rm max} = \left(\frac{0.3}{\epsilon_{\rm sfe}}\frac{17.3}{M_{\rm clump}} + 1.5 \times 10^{-3}\right)^{-0.77}. \quad (2)$$

For the clump MM1, assuming 30% star formation efficiency ($\epsilon_{\rm sfe}$), a high-mass star of 28 ± 9 $M_\odot$ can be formed.

(ii) Kauffmann & Pillai (2010) find an empirical high-mass star formation threshold, based on clouds with and without high-mass star formation. They suggest that IRDCs with masses larger than the mass limit given by $m_{\rm lim} = 580\,M_\odot\,(r/{\rm pc})^{1.33}$, where r is the source radius, are forming high-mass stars or will likely form them in the future. To be consistent with calculations made in our work, we use the factor of 580 directly obtained by using the Ossenkopf & Henning (1994) dust opacities and not the decreased (by a factor 1.5) dust opacities that lead to the original value of 870 (see Kauffmann & Pillai 2010 for details). Applying the Kauffmann & Pillai (2010) relationship to the clump MM1 ($r \approx 0.6$ pc), its corresponding mass threshold is 290 $M_\odot$, well below the measured mass of 1500 $M_\odot$. Thus, "the compactness" ($M_{\rm dust}/m_{\rm lim}$) of MM1 is 5.2, and it is highly likely that the clump will form high-mass stars.

Based on large samples of high-mass star-forming regions, Urquhart et al. (2014) and He et al. (2015) suggest that high-mass stars are formed in clumps with $\Sigma_{\rm clump} > 0.05$ gr cm^{-2}.

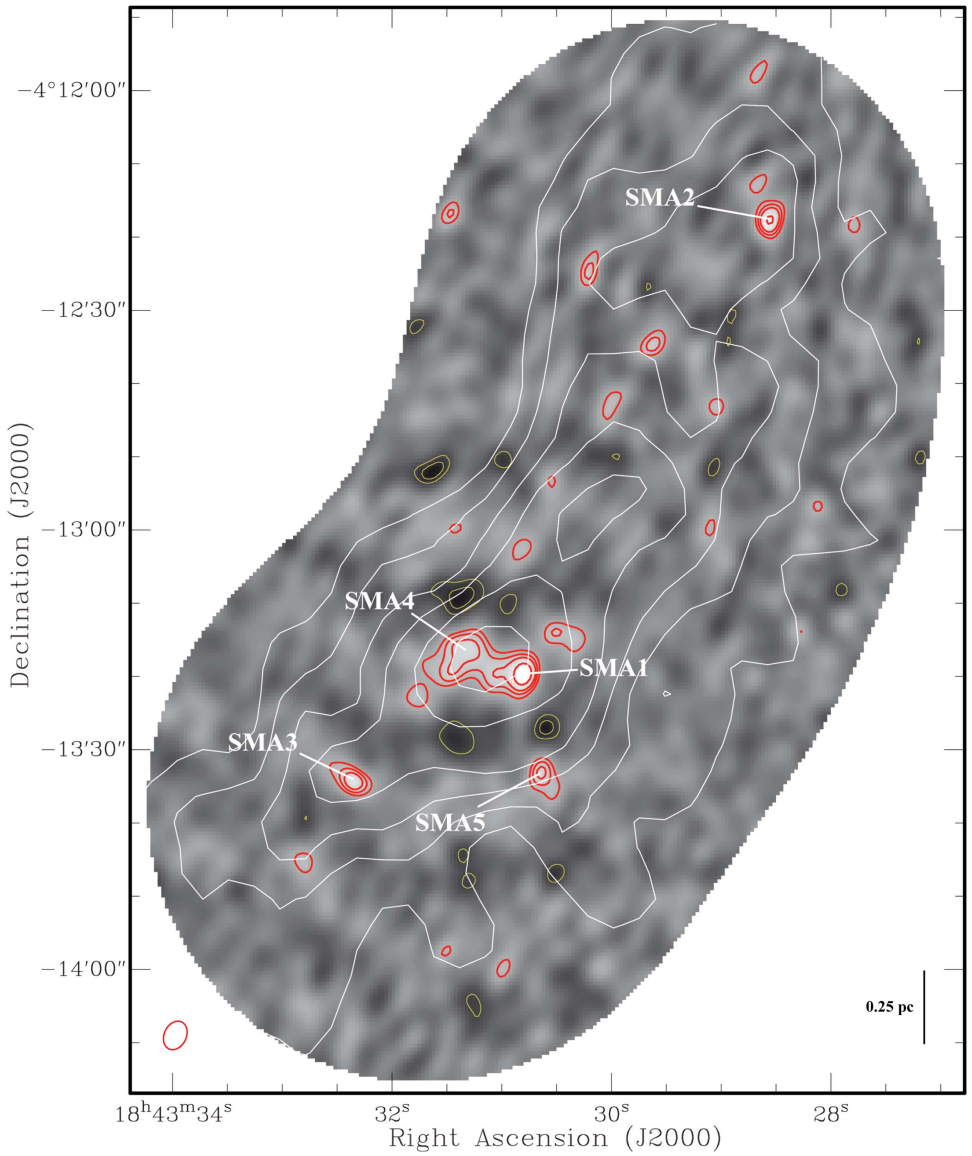

Figure 1. SMA 1.3 continuum emission ($\sim 3\farcs5$) in a grayscale image and red contours of IRDC G028.23-00.19 overlaid with 1.2 mm continuum emission from the IRAM 30 m telescope ($11''$) in white contours. Contour levels for the 1.3 continnum emission are -4, -3, 3, 4, 5, and 7 $\times$ σ, with σ equal to 0.75 mJ beam^{-1}. Contour levels for the 1.2 mm continuum emission are 20 ($\sim 3\sigma$), 35, 50, 65, 85, and 105 mJy beam^{-1}. The position of the five cores detected with SMA above 5σ are shown. The synthesized SMA beam is displayed at the bottom left of the image.

López-Sepulcre et al. (2010) suggest a significantly larger surface density threshold (0.3 gr cm^{-2}) for high-mass star formation based on the detection of massive outflows (outflow mass $>10\,M_{\odot}$). MM1 has $\Sigma_{\rm clump}$ and $\Sigma_{\rm peak}$ of 0.3 and 0.4 gr cm^{-2}, respectively. The surface density in MM1 was calculated as $\Sigma = M/(\pi r^2)$ with $r_{\rm clump} = 0.6$ pc and $r_{\rm peak} = 0.14$ pc using the IRAM 30 m dust continuum observations at $11''$ angular resolution (see Figure 1). The surface densities are significantly larger than the lower limit suggested for high-mass star formation and consistent with the highest threshold.

With a low virial parameter ($\alpha = 0.3$; Sanhueza et al. 2013), IRDC G028.23-00.19 MM1 is unstable and subject to collapse. Therefore, several pieces of evidence indicate that IRDC G028.23-00.19 will almost certainly form a stellar cluster including high-mass stars. The question that remains open is how. Since IRDC G028.23-00.19 MM1 appears to be in the prestellar stage and is likely to form high-mass stars, observations of this massive clump can be used to distinguish the early stage differences posited by high-mass star formation theories (see Section 1.1).

4. Results

4.1. Dust Continuum Emission

Figure 1 shows the 1.3 mm dust continuum emission from SMA ($\sim 3\farcs5$ angular resolution) in grayscale and red contours. White contours correspond to the 1.2 mm dust continuum emission from the single-dish IRAM telescope ($11''$ angular resolution). In the whole cloud, five SMA cores are detected above 5σ, which corresponds to 4.5 $M_{\odot}$ (following the procedure described in Section 5.4). The 5σ threshold was used because the sidelobe pattern produces negative artifacts with absolute values as large as 4σ, suggesting that some of the positive detections at 3σ and 4σ may be spurious sources due to

Table 1
SMA Core Parameters

Core Name	Position		Peak Flux	Integrated Flux	Angular Size	Deconvolved Size
	α(J2000)	δ(J2000)	(mJy beam^{-1})	(mJy)	($''$ × $''$)	($''$ × $''$)
SMA1	18:43:30.81	−04.13.19.6	8.18	12.2	4.8 × 3.8	2.8 × 2.1
SMA2	18:43:28.55	−04.12.17.6	8.14	10.2	4.5 × 3.4	2.2 × 1.1
SMA3	18:43:32.36	−04.13.34.3	5.35	7.04	4.5 × 3.6	2.0 × 1.9
SMA4	18:43:31.31	−04.13.16.4	5.29	9.28	…	…
SMA5	18:43:30.64	−04.13.33.1	4.80	6.97	5.0 × 3.6	3.1 × 1.5

Note. Fitting uncertainties are <1% for the peak flux, integrated flux, and the angular size, and <3% for the deconvolved size. For the calculation of physical properties, as discussed in Section 5.6, the uncertainties of flux and size measurements are dominated by the absolute flux scale of SMA (15%) and the distance to the source (10%). No 2D Gaussian fit was reliable for SMA4. In order to estimate its total flux, the flux inside the contour defined at 4σ was integrated. Its adopted size is the SMA synthesized beam.

side lobes instead of real sources. The cores are named SMA1, SMA2, SMA3, SMA4, and SMA5 in the order of decreasing peak flux (see Figure 1 and Table 1). Except for SMA4, all cores were fitted by 2D Gaussians in the CASA software package. The fitted parameters are listed in Table 1. The deconvolved size was adopted to determine the physical size of the cores. No 2D Gaussian fit succeeded for SMA4. The flux inside the contour defined at the 4σ level was used to estimate its integrated flux. To estimate the physical parameters of SMA4, we adopted the synthesized beam as the physical size. The parameters for SMA4 should be treated with caution because this core could be composed of a few unresolved condensations. SMA4 is not centrally peaked as the other SMA cores and it has approximately a constant brightness above the 5σ contour.

From Rathborne et al. (2010), the high-mass clump MM1 has a 1.2 mm single-dish integrated flux of 1.63 Jy. Comparing this integrated flux with the 1.3 mm SMA integrated flux of ∼80 mJy, ∼8% of the single-dish flux is recovered by the interferometer (assuming $\beta = 1.8$ to compare the somewhat different frequencies).

4.2. SiO and CO Emission

High-velocity gas in the SiO and CO lines is frequently interpreted as molecular outflows, and thus they can reveal deeply embedded active star formation that can be undetected at IR wavelengths. We searched for emission from the SiO (5-4) transition and found no detection in IRDC G028.23-00.19 MM1 at a sensitivity of 38 mJy beam^{-1} per channel of 1.1 km s^{-1}. The emission from the CO (2-1) transition is detected but the line profiles are heavily affected by self-absorption and/or missing flux. At a sensitivity of 40 mJy beam^{-1} per channel of 1.1 km s^{-1}, there is no evidence of wing emission that indicates protostellar outflows. Therefore, at the sensitivity level of these observations, we confirm that the cores embedded in the IRDC G028.23-00.19 MM1 clump are starless. Sanhueza et al. (2013) found SiO (2-1) emission to the north and south of MM1. With the SMA observations, we confirm the absence of molecular outflows and the more likely mechanisms for releasing SiO to the gas phase are large-scale shocks rather than active star formation.

4.3. NH_3 Emission

4.3.1. Images

Figure 2 shows, in colorscale, the moment 0 (integrated intensity) map of the five NH_3 hyperfine lines overlaid with the 1.3 mm dust continuum emission from SMA. The data above 2.5σ per channel were used for making the moment map. NH_3 emission is generally associated with dust emission, although the molecular emission is more spatially extended than the dust emission and is sometimes detected in regions without a dust counterpart.

The global, large-scale kinematics of the IRDC will be studied in detail in a following paper in which we will recover the missing flux by combining the NH_3 JVLA interferometric observations with the single-dish Green Bank telescope observations. In this paper, we focus on the compact cores detected in the prestellar, high-mass clump at the center of the IRDC.

Figure 3 shows an image of the central region containing four of the five SMA dust cores. This region corresponds to the central part of the massive clump MM1. The four panels show: (a) the moment 0 map of the 5 NH_3 (1, 1) hyperfines, (b) the NH_3 (2, 2) line, (c) the 4 NH_3 (1, 1) satellites, and (d) the NH_3 (1, 1) main component, in colorscale overlaid with black contours that correspond to the 1.3 mm dust continuum emission from the SMA. The NH_3 emission peaks do not overlap with the dust peaks, and remarkably, the NH_3 emission seems to avoid the dust cores (except in SMA5). This is more evident toward the SMA1 and SMA4 cores in panel (d). As can be seen in Figure 3, the NH_3 emission weakens toward the center of SMA1 and SMA4, independently of the transition used to make the moment map. This is likely produced for the combination of optical depth effects and depletion. The satellites could be self-absorbed and become weak toward the densest parts in the cores. The NH_3 (2, 2) may not be excited at the low temperatures near de core's centers. In addition, at the low temperatures and high densities of the core's centers, NH_3 could be frozen out onto dust grains.

4.3.2. Spectra

Figure 4 shows the NH_3 (1, 1) and (2, 2) spectra toward selected positions in the clump MM1. At the position of the SMA5, the NH_3 (1, 1) shows the normal relative intensity between the main component and the four satellites, i.e., the main component brighter than the satellites. At the position of the SMA1 and SMA4 cores, the main component is weaker than the satellites, while at the intermediate position labeled as "A" in Figure 3, the relative intensity among transitions is approximately unity.

The relative optical depths between the main NH_3 (1, 1) component and the satellites are determined by quantum mechanics according to their statistical weights. However, the

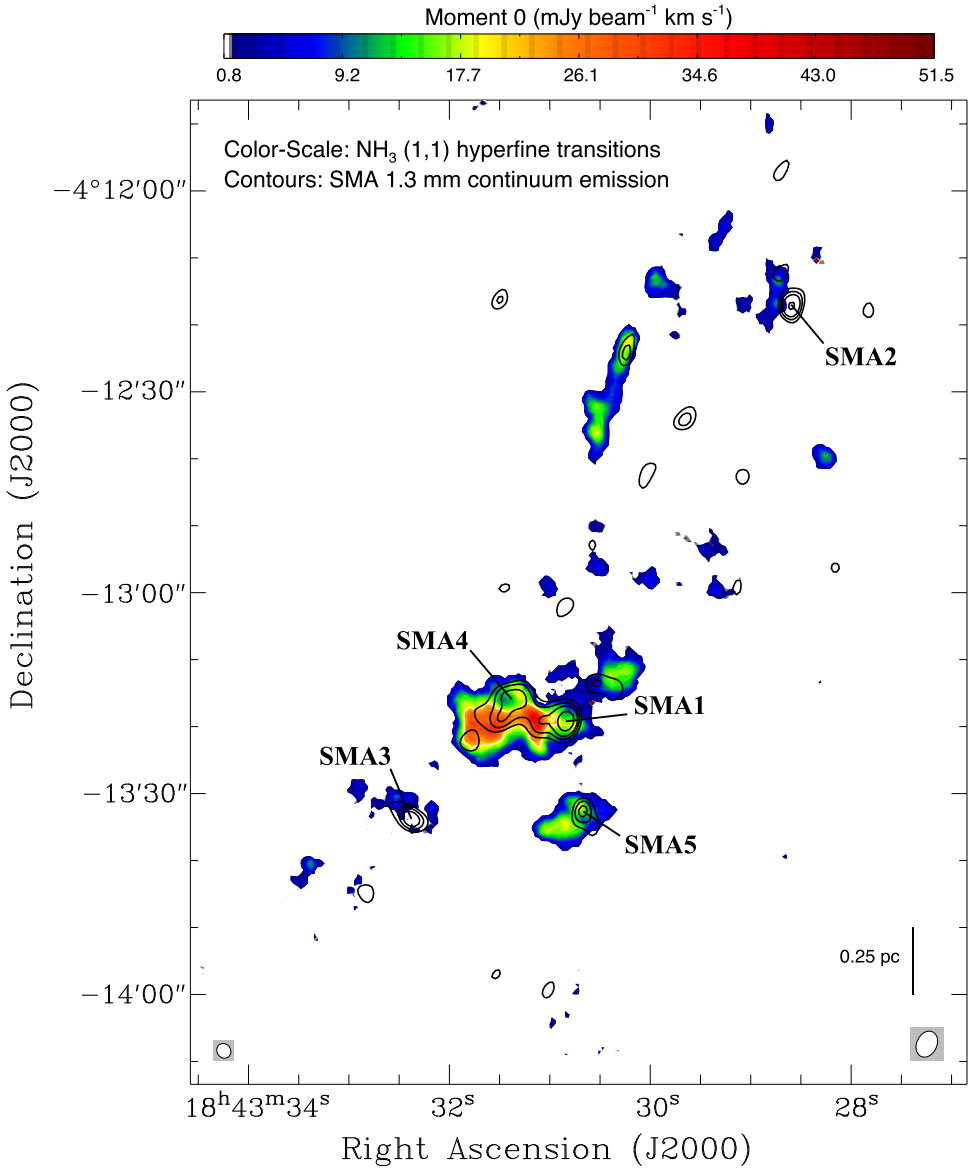

Figure 2. NH_3 moment 0 map (integrated intensity) in colorscale overlaid with 1.3 mm continuum emission from SMA in black contours. The moment 0 map includes the data above 2.5σ per channel for all five hyperfine lines. All emission above 15% of the peak emission is shown. Contour levels for the 1.3 continnum emission are 3, 4, 5, and 7 $\times$ σ, with σ equals to 0.75 mJ beam^{-1}. Angular resolutions of JVLA (2.″1) and SMA (3.″5) are shown in the bottom left and right, respectively.

observed relative intensity can be modified by optical depth effects: in the optically thin limit, the relative intensity will equal the ratio of the statistical weights, whereas in the optically thick limit, the relative intensity will equal 1. Toward some positions in the clump MM1, the relative intensity of $\sim$1 likely indicates high optical depths. However, an additional explanation is required to explain why in some places the main hyperfine component is weaker than the satellites. This unique feature is likely produced by the self-absorption of the cold gas in SMA1 and SMA4, as explained below.

The critical density of NH_3 (1, 1) is a few times 10^4 cm^{-3}. As determined in Section 5.4, the gas in the cores have densities of $\sim 10^6$ cm^{-3}. At these high densities, the gas in the cores should be thermalized and LTE should hold. As will be discussed in Section 5.1, the temperature of the gas derived by using single-dish telescopes and interferometers points to a common gas temperature of $\sim$12 K. Unfortunately, a direct estimation of the temperature at the position of the SMA dust cores with the JVLA NH_3 data cannot be made because the main (1, 1) component is less bright than its satellites. The emission from the main hyperfine is weaker than the satellites only at the position of the dust cores. This localized self-absorption rules out missing flux as a plausible explanation. Missing extended NH_3 emission would affect a much larger area and for no reason only specifically the dust cores.

If a point-like warmer source is deeply embedded in the SMA cores, the surrounding, colder medium could absorb the warmer emission. As a result, one would observe a spectrum with a similar shape to the observed SMA spectrum at the core positions, except that emission lines should be generally brighter than the surrounding, colder medium (especially the satellites). In the clump MM1, we see that the satellite lines decrease in intensity toward the dust cores, which is opposite to that expected if there is an embedded warmer source.

On the other hand, to explain the abnormal NH_3 profile, we suggest that the more diffuse (3×10^4 cm^{-3}) gas/dust in the

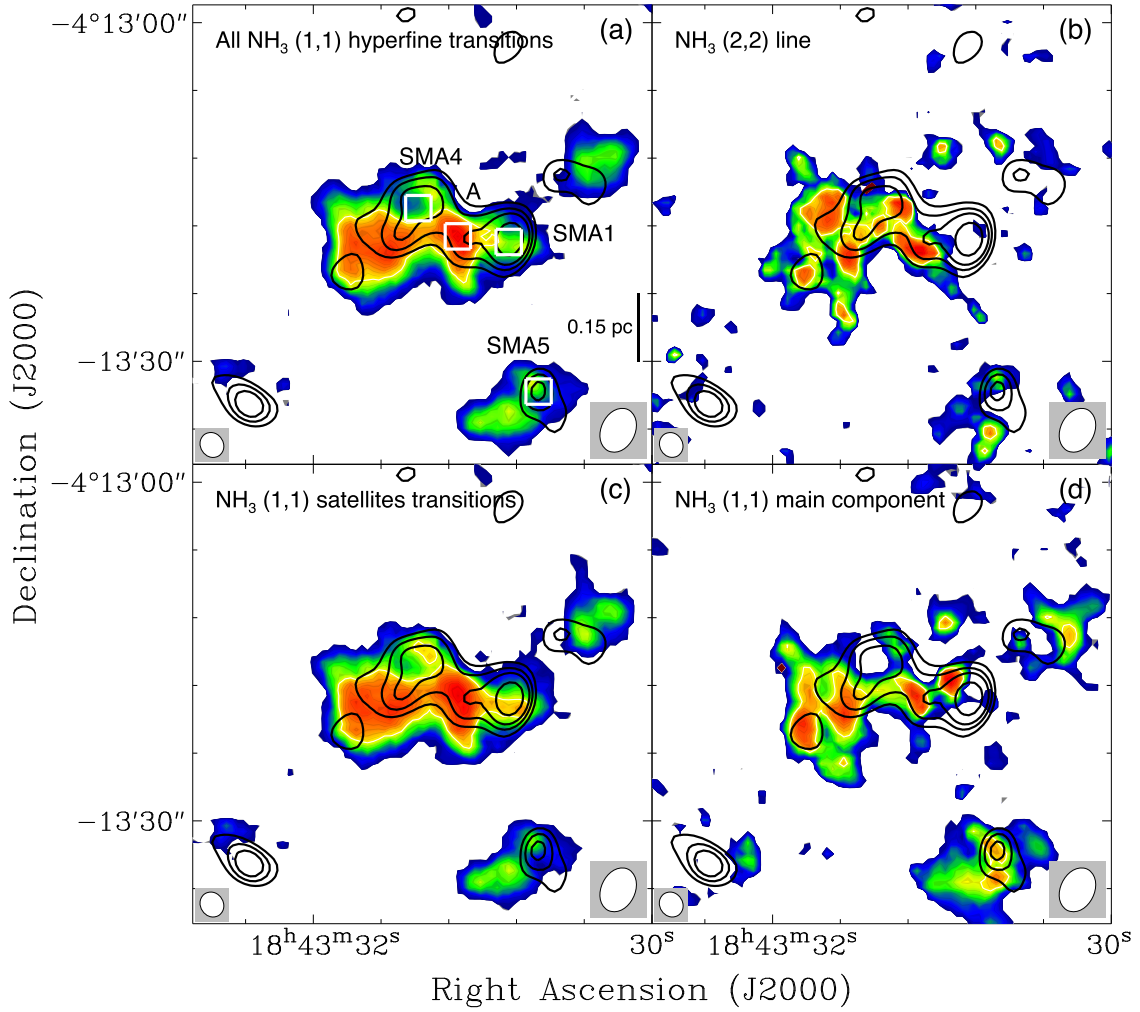

Figure 3. NH_3 moment 0 map (integrated intensity) in colorscale overlaid with 1.3 mm continuum emission from SMA in black contours toward the central region of the IRDC. Panel (a) corresponds to all five NH_3 (1, 1) hyperfine lines. Panel (b) corresponds to the NH_3 (2, 2) line. Panel (c) corresponds to the four NH_3 (1, 1) satellites. Panel (d) corresponds to the NH_3 (1,1) main component. The moment 0 map includes the data above 2.5σ per channel. All emission above 20% of the peak emission is shown. Contour levels for the 1.3 continnum emission are 3, 4, 5, and 7 × σ, with σ equals to 0.75 mJ beam^{-1}. Angular resolutions of JVLA (2.″1) and SMA (3.″5) are shown in the bottom left and right, respectively. White boxes show the positions of the spectra displayed in Figure 4.

IRDC is at ∼12 K, whereas the material in the dense cores is colder (<12 K). Thus, from our line of sight, we see that the cold core gas absorbs the background warmer, more diffuse IRDC gas. In this picture, we assume that the surrounding medium is not symmetrically distributed around the cores and that there is an excess of background IRDC gas with respect to foreground IRDC gas. The peculiarity of the NH_3 spectra at the position of SMA1 and SMA4 would be the result of cold gas without internal heating sources, supporting the starless status of the cores.

4.3.3. Line Widths

Line[9] widths are required to determine the turbulence of the gas, the virial mass, and the virial parameter. A multi-Gaussian function with fixed frequency separation between hyperfine transitions was fitted to an averaged spectra of 25 pixels (approximately the NH_3 beam size) centered on the SMA core positions. The line widths of the outer left hyperfine ($JKF_1 = 111 \rightarrow 110$) associated with each SMA core are displayed in Table 2. When line widths approach the thermal line width (∼0.2 km s^{-1} at 12 K), the magnetic hyperfine splitting can be resolved (e.g., Rydbeck et al. 1977), except for the outer left hyperfine. The two magnetic hyperfine transitions that form part of the outer left hyperfine are only separated by 0.14 km s^{-1} (11 kHz) and may be barely resolved in cold, low-mass star-forming regions. In IRDC G028.23-00.19, all other hyperfines show 20% or larger line widths than the one measured for the outer left hyperfine, indicating that the magnetic hyperfine splitting is becoming relevant at the line widths observed in this IRDC (although they are not resolved). The observed line widths ($\Delta V_{\rm obs}$) of the outer left hyperfine displayed in Table 2 have an average of 0.9 km s^{-1}, which is roughly twice the channel width of the observations (0.4 km s^{-1}). The deconvolved line width ($\Delta V_{\rm dec}$) in km s^{-1} is determined following $\Delta V^2_{\rm dec} = \Delta V^2_{\rm obs} - 0.4^2$. Calculated values are displayed in Table 2. The deconvolved line width is 10% to 20% lower than the observed line width and will be used for the determination of core's properties.

The intrinsic line width ($\Delta V_{\rm int}$) of a line can be broadened by the line optical depth. As will be discussed in Section 5.1, the optical depth of the outer left hyperfine is at least ∼2.4 at the

[9] We refer to line width (ΔV) to the full width half maximum (FWHM) of molecular line emission. The line width relates to the velocity dispersion (σ) by $\Delta V = 2\sqrt{2\ln 2}\ \sigma \approx 2.35\sigma$.

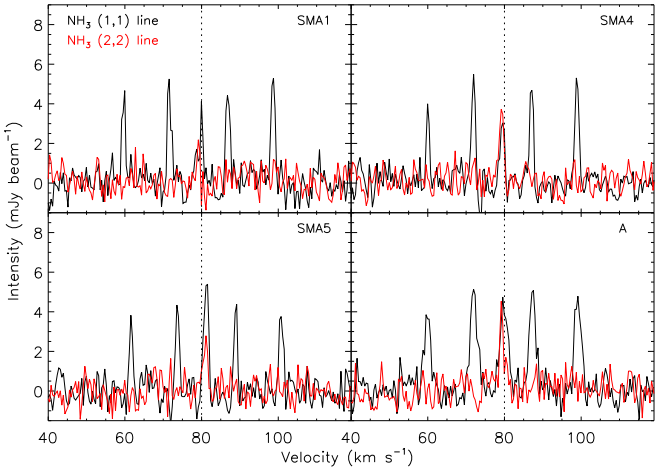

Figure 4. NH_3 (1, 1) spectra (in black) toward the clump MM1 showing lines with high optical depths and self-absorption. NH_3 (2, 2) spectra are shown in red for comparison. Position A is indicated in Figure 3. The dotted line shows the V_{LSR} of the IRDC (80 km s^{-1}).

Table 2
Measured and Derived Line Widths Associated with the SMA Cores

Core Name (1)	ΔV_{obs} (km s^{-1}) (2)	ΔV_{dec} (km s^{-1}) (3)	ΔV_{int} (km s^{-1}) (4)	ΔV_{nt} (km s^{-1}) (5)	Mach Number (6)
SMA1	1.02 ± 0.15	0.91 ± 0.16	<0.65	0.89	1.8
SMA2	0.68 ± 0.18	0.55 ± 0.22	<0.39	0.52	1.1
SMA3	0.75 ± 0.25	0.63 ± 0.29	<0.45	0.61	1.3
SMA4	0.94 ± 0.12	0.85 ± 0.13	<0.60	0.83	1.7
SMA5	0.95 ± 0.17	0.86 ± 0.19	<0.61	0.84	1.8

Note. Columns (2)–(4) correspond to line widths of the NH_3 outer left hyperfine. ΔV_{obs} is the observed line width. ΔV_{dec} is the deconvolved line width given by $\Delta V_{dec}^2 = \Delta V_{obs}^2 - 0.4^2$, where 0.4 km s^{-1} is the spectral resolution. ΔV_{dec} will be used to calculate the physical parameters of the SMA cores. ΔV_{int} is the intrinsic line width given by Equation (3). Column (5) is the non-thermal component of the NH_3 determined from ΔV_{dec}, assumed to be the same as the non-thermal component of H_2. In column (6), the Mach number is calculated using $\Delta V_{nt}/\Delta V_{th}$, where $\Delta V_{th} = 0.48$ km s^{-1} corresponds to the H_2 thermal line width.

SMA core positions. Fitting a Gaussian profile to an optically thick or moderately thick line will result in an overestimation of the real velocity dispersion of the gas. To correct for this effect, the following expression can be used (e.g., Beltrán et al. 2005):

$$\frac{\Delta V_{dec}}{\Delta V_{int}} = \frac{1}{\sqrt{\ln 2}} \sqrt{-\ln\left[-\frac{1}{\tau}\ln\left(\frac{1+e^{-\tau}}{2}\right)\right]}, \quad (3)$$

where ΔV_{int} profile is assumed to be Gaussian. Adopting $\tau = 2.4$, the correction for optical depth produces intrinsic line widths ∼30% smaller (see Table 2). We prefer to use ΔV_{dec} over ΔV_{int} in the following calculations because the uncertainty in τ is large (which propagate to ΔV_{int}, virial masses, and virial parameters). However, we stress that large optical depths will make ΔV_{int} smaller, which produces virial masses and virial parameters lower than that calculated with ΔV_{dec}. If ΔV_{int} is used, our final conclusions do not change, rather they are reinforced.

5. Analysis

5.1. NH_3 Optical Depth and Rotational Temperature

The calculation of several physical parameters depends on the temperature of the medium. In this section, we define the temperature that will be used for the calculation of physical parameters in the following sections.

The optical depth of the NH_3 hyperfine lines can be derived by taking the ratio between the main and the satellite hyperfine components (assuming they have the same filling factor), following, for example, Sanhueza et al. (2012):

$$\frac{1-e^{-\tau_{(1,1,m)}}}{1-e^{-\gamma\tau_{(1,1,m)}}} = \frac{T_{b(1,1,m)}}{T_{b(1,1,s)}}, \quad (4)$$

where $T_{b(1,1,m)}$ and $T_{b(1,1,s)}$ are the brightness temperatures of the main and satellites components, respectively. The factor γ is the relative strength determined by the statistical weights. The value of γ is $1/3.6$ for the two inner satellites and $1/4.5$ for the two outer satellites (Rydbeck et al. 1977; Ho & Townes 1983).

The rotational temperature, T_R, that characterizes the population distribution between the (1, 1) and (2, 2) states can be determined by (Ho & Townes 1983)

$$T_R = -\frac{41.5}{\ln\left[0.282\left(\frac{\tau_{(2,2,m)}}{\tau_{(1,1,m)}}\right)\right]} \text{ K}, \quad (5)$$

where $\tau_{(2,2,m)}$ can be determined from

$$\frac{1-e^{-\tau_{(1,1,m)}}}{1-e^{-\tau_{(2,2,m)}}} = \frac{T_{b(1,1,m)}}{T_{b(2,2,m)}}. \quad (6)$$

The determination of the optical depth and rotational temperature becomes unreliable when the the intensity ratio between $T_{b(1,1,m)}$ and $T_{b(1,1,s)}$ approaches unity and impossible when the main NH_3 component is weaker than the satellites. As discussed earlier, NH_3 profiles with these odd characteristics are repeatedly seen in IRDC G028.23-00.19, especially in the clump MM1. Thus, optical depths and rotational temperatures were determined only in a few positions, and the mean values associated with the SMA cores will be reported. These mean values were determined inside the contour defined by the 5σ level in the dust continuum emission. The mean optical depth of the NH_3 (1, 1) main component is 11, demonstrating that ammonia emission is optically thick. The mean optical depths of the NH_3 (1, 1) satellites and NH_3 (2, 2) main component are moderately optically thick with values of 2.4 and 1.2, respectively. All these optical depths values should be treated as lower limits for the SMA cores since, at the center of the cores, exact values cannot be determined due to the extremely high optical depths.

The mean rotational temperature is 13 K. This value corresponds to an upper limit because at higher optical depths, the temperature is lower. Dirienzo et al. (2015) also estimate ∼13 K using lower angular resolution observations of NH_3. This temperature is within the uncertainties quoted by the other two methods used for temperature determination. Both the *Herschel* dust temperature and the temperature derived by the rotational technique using CH_3OH are 12 ± 2 K (Sanhueza et al. 2013). This latter value, 12 ± 2 K, will be adopted for the rest of this work.

5.2. Jeans Mass, Free Fall Time, and Dynamical Crossing Time of the MM1 Clump

Here, we calculate the Jeans mass to compare with the measured core masses in the MM1 clump. The comparison between the free fall time and the dynamical crossing time can give additional information on the dynamical state of the clump.

If the fragmentation of a clump is governed by the Jeans instability, the initially homogeneous gas will fragment into smaller pieces defined by the Jeans length (λ_J) and the Jeans mass (M_J):

$$\lambda_J = \sigma_{\rm th}\left(\frac{\pi}{G\rho}\right)^{1/2}, \quad (7)$$

and

$$M_J = \frac{4\pi\rho}{3}\left(\frac{\lambda_J}{2}\right)^3 = \frac{\pi^{5/2}}{6}\frac{\sigma_{\rm th}^3}{\sqrt{G^3\rho}}, \quad (8)$$

where ρ is the mass density and $\sigma_{\rm th}$ is the thermal velocity dispersion (or isothermal sound speed, c_s) given by

$$\sigma_{\rm th} = \left(\frac{k_{\rm B}T}{\mu m_{\rm H}}\right)^{1/2}. \quad (9)$$

The thermal velocity dispersion is mostly dominated by H_2 and He, and it should be derived by using the mean molecular weight per free particle, $\mu = 2.37$ (Kauffmann et al. 2008). The thermal line width of the total gas ($\Delta V_{\rm th} = 2\sqrt{2\ln 2}\ \sigma_{\rm th}$) is 0.48 km s^{-1}. Assuming a mass density given by a spherical clump of mass 1500 $M_\odot$ and radius of 0.6 pc (Sanhueza et al. 2013), the thermal Jeans length and mass of MM1 are 0.14 pc and 2.2 $M_\odot$, respectively. If we replace $\sigma_{\rm th}$ by the observed velocity dispersion ($\sigma_{\rm obs}$) in the MM1 clump, we can obtain the turbulent Jeans mass. Using the NH_2D (1-1) line width of 1.9 km s^{-1} ($\sigma_{\rm obs} = 0.81$ km s^{-1}) observed on clump scales by Sanhueza et al. (2013), we obtain a turbulent Jeans mass of the clump of 130 $M_\odot$.

The characteristic time for gravitational collapse (ignoring thermal pressure, turbulence, and magnetic fields), known as the free fall time, is given by

$$t_{\rm ff} = \sqrt{\frac{3\pi}{32G\rho}}, \quad (10)$$

and the dynamical crossing time, which depends on the radius of the clump (R) and its gas velocity dispersion ($\sigma_{\rm obs}$), is given by $t_{\rm dyn} = R/\sigma_{\rm obs}$. The free fall time and the dynamical crossing time of MM1 are 2.0×10^5 years and 7.3×10^5 years, respectively. A clump becomes gravitationally unstable if $t_{\rm ff} < t_{\rm dyn}$ (e.g., Contreras et al. 2017). The $t_{\rm ff}/t_{\rm dyn}$ ratio is 0.3, indicating gravitational contraction.

5.3. Non-thermal Component of the SMA Cores

The level of turbulence in the cores can be compared with the turbulence suggested by some high-mass star formation theories. Assuming that the NH_3 emission traces the velocity dispersion in the interior of the SMA cores, the non-thermal component ($\Delta V_{\rm nt}$) can be estimated using $\Delta V_{\rm dec}$ from the outer left hyperfine and the relation $\Delta V_{\rm dec}^2 = \Delta V_{\rm th}^2 + \Delta V_{\rm nt}^2$. The thermal line width ($\Delta V_{\rm th}$) for NH_3 is 0.18 km s^{-1} at 12 K. Because the non-thermal component is independent of the observed line from which it is determined (except for molecular outflow/shock tracers), the determined $\Delta V_{\rm nt}$ from NH_3 represents the turbulent motions from the total gas in the cores (mostly H_2). $\Delta V_{\rm nt}$ ranges from 0.52 to 0.89 km s^{-1}. The thermal line width of the total gas (for $\mu = 2.37$) is 0.48 km s^{-1}, leading to Mach numbers of ($\Delta V_{\rm nt}/\Delta V_{\rm th} \sim 1.1$–1.8). If $\Delta V_{\rm int}$ is used instead of $\Delta V_{\rm dec}$, a lower non-thermal component that is just 0.7–1.3 times the thermal line width is derived. $\Delta V_{\rm nt}$ and Mach numbers ($\Delta V_{\rm nt}/\Delta V_{\rm th}$) are given in Table 2.

5.4. SMA Cores' Properties Using Dust Continuum Emission

The core mass is determined to search for the existence of high-mass cores and compare with the thermal and turbulent Jeans masses. The mass of the cores was calculated using the following expression:

$$M_{\rm core} = \mathbb{R}\frac{F_\nu D^2}{\kappa_\nu B_\nu(T)}, \quad (11)$$

where F_ν is the measured integrated source flux, $\mathbb{R}$ is the gas-to-dust mass ratio, D is the distance to the source, κ_ν is the dust opacity per gram of dust, and B_ν is the Planck function at the dust temperature T. A value of 0.9 cm^2 g^{-1} is adopted for $\kappa_{1.3\,\rm mm}$, which corresponds to the opacity of dust grains with thin ice mantles at gas densities of 10^6 cm^{-3} (Ossenkopf & Henning 1994). A gas-to-dust mass ratio of 100 was assumed in this work. The number density was calculated by assuming a spherical core and using the molecular mass per hydrogen molecule ($\mu_{\rm H_2}$) of 2.8 (Kauffmann et al. 2008). Masses, number densities, and surface densities for all cores are listed in Table 3.

5.5. Dynamical State of Embedded Cores

The dynamical state of the cores is assessed by determining the virial mass and the virial parameter in order to compare with model predictions. The virial mass was evaluated according to the prescription of MacLaren et al. (1988; neglecting magnetic fields and external pressure):

$$M_{\rm vir} = 3\left(\frac{5-2n}{3-n}\right)\frac{R\sigma^2}{G}, \quad (12)$$

where R is the radius of the core, σ is the velocity dispersion along the line of sight, G is the gravitational constant, and n is a constant whose exact value depends on the density profile, $\rho(r)$, as a function of the distance from the core center, $\rho(r) \propto r^{-n}$.

Equation (12) can be written in more useful units as

$$M_{\rm vir} = k\left(\frac{R}{[\rm pc]}\right)\left(\frac{\Delta V}{[\rm km\ s^{-1}]}\right)^2 M_\odot, \quad (13)$$

where ΔV is the line width and the value of k depends on the density profile (MacLaren et al. 1988). For a uniform density profile, k is equal to 210. However, the uniform density profile is unlikely and represents an upper limit for the virial mass. In fact, Garay et al. (2007) and Mueller et al. (2002) find, on average, a radial profile index of 1.8 in high-mass star-forming

Table 3
Measured Properties of the SMA Cores

Core Name	R[a] (pc)	$M_{\rm core}$ ($M_\odot$)	$M_{\rm core}/M_J$[b]	$n(H_2)$ ($\times 10^6$ cm^{-3})	Σ (g cm^{-2})	$\Delta V_{\rm dec}$ (km s^{-1})	$M_{\rm vir}$[c] ($M_\odot$)	α
SMA1	0.030	15	6.8	1.9	1.1	0.91	3.7 ± 1.4	0.25 ± 0.15
SMA2	0.019	12	...	6.0	2.2	0.55	0.85 ± 0.70	0.07 ± 0.06
SMA3	0.024	8.5	3.9	2.1	1.0	0.63	1.4 ± 1.3	0.2 ± 0.2
SMA4	0.043	11	5.0	0.5	0.40	0.85	4.6 ± 1.5	0.41 ± 0.23
SMA5	0.027	8.4	3.8	1.5	0.78	0.86	2.9 ± 1.3	0.35 ± 0.22

Notes. Uncertainties for the radius (R), mass of the core ($M_{\rm core}$), volume density ($n(H_2)$), and surface density (Σ) are 10%, 49%, 48%, and 47%, respectively (see discussion in Section 5.6). Uncertainty for $\Delta V_{\rm dec}$ is given in Table 2. $M_{\rm vir}$ and α correspond to the virial mass and virial parameter, respectively.
[a] This radius (R) corresponds to half of the deconvolved size quoted in Table 1. For SMA4, the radius is half of the synthesized beam.
[b] The Jeans mass of the clump MM1 is 2.2 $M_\odot$ (see Section 5.2). SMA2 is not embedded in MM1.
[c] Virial mass estimated by assuming a density distribution $\propto r^{-1.8}$.

regions. The same average value for the radial profile index is also found on IRDC cores by Zhang et al. (2009). A density profile with $n = 1.8$, resulting in $k = 147$, will be used in this work. The virial parameter (α) was determined by taking the ratio between Equations (11) and (13): $\alpha = \frac{M_{\rm vir}}{M_{\rm core}}$. The calculated $M_{\rm vir}$ and α are listed in Table 3.

5.6. Uncertainties in the Determination of Physical Parameters

There are several sources of uncertainty in the mass determination of star-forming regions. This section discusses the uncertainties associated with the parameters involved in the mass determination.

The difficulty of characterizing interstellar dust makes κ_ν the least-known parameter for determining the core mass. In the literature, the models of Ossenkopf & Henning (1994) are broadly used and have been favored in multi-wavelength observations of star-forming regions (e.g., Shirley et al. 2011). The value of κ_ν used in this work (0.9 cm^2 g^{-1}) corresponds to the so-called OH5 grain which is covered by a thin layer of ice mantle and coagulated at gas densities of 10^6 cm^{-3} (Ossenkopf & Henning 1994). The value of κ_ν ranges from 0.7 to 1.05 if the values for thick layers and densities of 10^5 and 10^7 cm^{-3} are used instead. Assuming that the range of values is uniformly distributed between 0.7 and 1.05, the standard deviation can be determined by taking the size of the range (1.05–0.7 = 0.35) divided by $\sqrt{12}$. The value obtained is 0.1. Then, assuming 1σ uncertainty, κ_ν would be 0.9 ± 0.1 (11% uncertainty). Shirley et al. (2011) constrain theoretical models of dust opacity at 450 and 850 μm. The OH5 model is one of three supported by the observations. Shirley et al. (2011) determine several values for $\kappa_{450\,\mu\rm m}$ and $\kappa_{850\,\mu\rm m}$. Assuming that the range of values they obtain is uniformly distributed between the extreme values, the standard deviation is 1.8 (28% of $\kappa_{450\,\mu\rm m} = 6.4$ from the OH5 model) and 0.34 (19% of $\kappa_{850\,\mu\rm m} = 1.8$ from the OH5 model). To be conservative, overall, a 1σ uncertainty of 28% will be adopted for $\kappa_\nu = 0.9$ at 1.3 mm.

Another difficulty in determining the core mass is the conversion factor that relates the dust with the gas mass. The value of the canonical gas-to-mass ratio ($\mathbb{R}$) widely used is 100. Depending on the grain size, shape, and composition, determinations of the Galactic dust-to-gas mass ratio range between 70 and 150 (e.g., Devereux & Young 1990; Vuong et al. 2003). In this work, the canonical value of 100 has been adopted. Assuming that the range of $\mathbb{R}$ is uniformly distributed between 70 and 150, the standard deviation is 23. Thus, the 1σ uncertainty for the gas-to-mass ratio is 23 (23% of $\mathbb{R} = 100$).

The dust temperature and measured continuum flux have an uncertainty of 17% (see Section 5.1) and 15% (see Section 2.1), respectively. The major source of error in the kinematic distance method is the assumption of circular motions. Non-circular motions, e.g., cloud–cloud velocity dispersion (random motions), will lead to velocity perturbations of about 5 km s^{-1}. Using the rotation curve of Clemens (1985), IRDC G028.23-00.19 is located at 5.1 kpc. Varying the velocity of G028.23-00.19 in ±5 km s^{-1}, an uncertainty in the distance of 10% is estimated. Another rotation curve places the IRDC at a distance of 4.6 kpc (Reid et al. 2009). In this work, the rotation curve of Clemens (1985) will be adopted; the distance derived by using the rotation curve of Reid et al. (2009) agrees within the uncertainties.

Due to their poor characterization, κ_ν and $\mathbb{R}$ add an "intrinsic" uncertainty of 32% to the mass determination of cores. Depending on how well the flux, distance, and temperature of the sources are determined, the uncertainty in the mass can be even higher than a factor of 2. Because the SMA cores are observed with the same instrument, are at the same distance, and have the same temperature, all the SMA cores have the same mass uncertainty of 49%. Due to the lower dependence on distance, the uncertainty for the volume density and surface density is 48% and 47%, respectively.

The uncertainty in the NH_3 line widths, and their effects on the virial mass and the virial parameter, will be different for each core. On average, line widths, virial masses, and virial parameters have 30%, 60%, and 75% uncertainties. The uncertainties for each individual core are quoted in Table 3.

6. Discussion

6.1. Implications for High-mass Star Formation in IRDC G028.23-00.19

6.1.1. High-mass Prestellar Cores

Recent works have focused on determining the mass of prestellar cores embedded in massive cluster-forming clumps in order to test theoretical models (e.g., Pillai et al. 2011; Tan et al. 2013; Zhang et al. 2015). However, the definition of a bona fide "prestellar, high-mass core" is rather vague. Longmore et al. (2011) suggest that in order to form an O-type star through the direct collapse of a core, the core should have of the order of 100 $M_\odot$. Tan et al. (2014) suggest that prestellar, high-mass cores should have ∼100 Jeans masses. Krumholz et al. (2007b) simulate the formation a high-mass star of 9 $M_\odot$ from a

turbulent, virialized core of 100 $M_\odot$ and 0.1 pc. It seems clear that a prestellar, high-mass core should have several tens of solar masses. So far, no prestellar cores have been detected with such a large mass. Indeed, follow-up observations of many suggested high-mass starless core candidates revealed molecular outflows or maser emission, irrefutable signs of star formation (e.g., Bontemps et al. 2010; Duarte-Cabral et al. 2013; Tan et al. 2013; Shipman et al. 2014; Feng et al. 2016b; Tan et al. 2016).

To be conservative, in this work we define a high-mass core as a core with a mass larger than $\sim$30 $M_\odot$. This definition is consistent with the star formation efficiency of 30% derived by Alves et al. (2007) in the Pipe dark cloud (also tentatively determined in the Cygnus X complex by Bontemps et al. 2010), assuming that the initial mass function is a direct product of the CMF as stated for the turbulent core accretion model, e.g., Tan et al. (2014). Interestingly, the prestellar core candidate MM2 embedded in the active high-mass star-forming region G11.92-0.61 (Cyganowski et al. 2014, 2017) satisfies this condition and stands out as a good candidate to be a high-mass prestellar core. We note that in our definition of high-mass core, we have not considered that $\sim$80% of high-mass stars are found in binary systems (Kouwenhoven et al. 2005; Chini et al. 2012) and that the majority of the systems contain pairs of similar mass.

The cores found in IRDC G028.23-00.19 have gas masses ranging from 8 to 15 $M_\odot$. We therefore find no high-mass cores that currently have the mass reservoir to form a high-mass star, in disagreement with the core accretion model.

6.1.2. Fragmentation

Dust and gas in IRDC G028.23-00.19 MM1 seem to be cold and quiescent. Contreras et al. (2017) find that massive clumps are more susceptible to gravitational instabilities and evolve faster than low-mass clumps, based on the low $t_{\rm ff}/t_{\rm dyn}$ ratio. The low virial parameter and low $t_{\rm ff}/t_{\rm dyn}$ ratio indicate that MM1 has started gravitational contraction and is not a transient object. Indeed, at high angular resolution, the first members of the future stellar cluster are revealed through dust continuum emission. At the sensitivity observed with SMA, no molecular outflows are detected and the cores embedded in this massive clump seem to be in the prestellar phase. Considering that the current observational evidence supports the idea that the IRDC will form high-mass stars, the lack of high-mass prestellar cores (>30 $M_\odot$) have important implications in the formation of high-mass stars.

Krumholz & McKee (2008) suggest that the heating produced by accreting low-mass stars in regions with surface densities $\geqslant$1 g cm^{-2} can halt fragmentation by increasing the Jeans mass. Although surface densities of the order of 1 g cm^{-2} are found at core scales in IRDC G028.23-00.19, only low temperatures are measured and there are no signs of active star formation. A similar conclusion was also reported in Zhang et al. (2009) and Wang et al. (2012), who studied a massive clump in IRDC G28.34+0.06 and found low gas temperatures of $\sim$14 K toward dense cores. In order to have a Jeans mass of 30 $M_\odot$ in IRDC G028.23-00.19 MM1, a temperature of 70 K would be needed. We note that heating from protostars seems unimportant even in G11.92-0.61, the high-mass star-forming region hosting a high-mass prestellar core candidate with a hot core nearby (Cyganowski et al. 2014). The measured temperature in the high-mass prestellar core candidate is 17–19 K. Magnetic fields have also been suggested as important to suppress fragmentation (Commerçon et al. 2011; Myers et al. 2013). However, to date, there are no measurements of the magnetic field in high-mass prestellar clump candidates, including IRDC G028.23-00.19.

The Jeans mass in IRDC G028.23-00.19 MM1 is 2.2 $M_\odot$. The observed SMA cores are 4–7 times more massive. The observational fact that core masses are larger than the Jeans mass is inconsistent with competitive accretion models, unless (i) we are not witnessing the initial fragmentation of the clump and the initial Jeans cores have had sufficient time to accrete and grow to reach their current masses or (ii) these cores could still fragment in smaller objects if higher angular resolution observations were available. We note that SMA observations are not sufficiently sensitive ($5\sigma = 4.5\,M_\odot$) to detect Jeans cores, and we cannot exclude the possibility of a core population with lower masses separated by the Jeans length (λ_J). The Jeans length in MM1 is 0.14 pc and the separation among the SMA cores is larger than $2\lambda_J$.

With the largest core mass of 15 $M_\odot$, our observations disagree with the predictions from the turbulent core accretion model; high-mass prestellar cores are not found. The turbulent Jeans mass in IRDC G028.23-00.19 MM1 (130 $M_\odot$) is much larger than the core masses (nine times larger than the most massive core). Therefore, contrary to other slightly more evolved IRDCs (e.g., Wang et al. 2011, 2014; Lu et al. 2015), turbulence supported fragmentation does not seem to be the dominant process controlling the early stages of high-mass stars and cluster formation. Both the thermal Jeans mass and the turbulent Jeans mass may be too simple descriptions to explain the fragmentation of massive clumps. A larger sample will be key to confirm if this is a general trend at the very early stages of high-mass star formation evolution, or if IRDC G028.23-00.19 is a unique case where neither thermal pressure nor turbulent pressure dominate the fragmentation of a massive cluster-forming clump.

6.1.3. Turbulence

The importance of turbulence can be further investigated by calculating the Mach number. As asserted by McKee & Tan (2003), one of the most important premises of the turbulent core accretion model is that cores that will form high-mass stars are highly supersonically turbulent, leading to virial equilibrium ($\alpha \sim 1$). NH_3 lines have narrow line widths in IRDC G028.23-00.19 ($\lesssim$1.0 km s^{-1}). With Mach numbers ($\Delta V_{\rm nt}/\Delta V_{\rm th}$) of $\sim$1.1–1.8, the total gas is transonic and mildly supersonic. Although the gas may be slightly affected by turbulence, it is not highly supersonic (Mach numbers >5) as suggested by McKee & Tan (2003) and Krumholz et al. (2007a, 2007b). If optical depth is taken into consideration for the outer left NH_3 hyperfine, the $\Delta V_{\rm int}$ would produce an even lower non-thermal component that would be just 0.7–1.3 times the thermal line width (subsonic–transonic).

The simple analytic models developed by Myers (2011, 2014) describe how a protostar gains mass from the collapse of a thermally supported core and from accretion of a turbulent clump. These models, based on statistical arguments, have a combination of "core-fed" and "clump-fed" components, which represent isothermal collapse and reduced Bondi accretion. The duration of the accretion is more important than the initial core mass in settling the final mass of stars. Myers (2011, 2014) suggests that the cores and the protostars that will become high-mass stars at the end of the cluster formation are born earlier than the low-mass counterparts from low-mass thermal cores.

Stars become massive after accreting both thermal core gas and turbulent clump gas. Relatively low Mach numbers in the SMA cores in IRDC G028.23-00.19 may hint at some similarity to the work of Myers (2011, 2014). Myers (2014) suggests that by the time that high-mass stars are identified, the core gas is turbulent because (i) its clump origin and (ii) the star itself injects energy into the core (by heating, winds, and/or ionization). The SMA cores may have already accreted a substantial amount of material from the clump, increasing the mass and turbulence in agreement with Myers (2014). However, we have no concrete evidence to support or refute that this scenario is occurring in IRDC G028.23-00.19.

6.1.4. Dynamical State of the Cores

The low turbulence level strongly affects the dynamics of the cores. Turbulent gas motions, and magnetic fields as well, can provide additional support against self-gravity. Considering only turbulence, all SMA cores consistently show $\alpha < 0.5$, and are hence subvirial. These values suggest that in the absence of magnetic fields, the SMA cores are strongly subvirial and simultaneously collapsing along with the whole clump that has $\alpha = 0.3$. This scenario of global collapse dominated by subvirialized structures is consistent with some models of competitive accretion (e.g., Wang et al. 2010) and inconsistent with the turbulent accretion model (McKee & Tan 2003; Tan et al. 2014). According to competitive accretion scenarios, the low–intermediate-mass cores in IRDC G028.23-00.19 could grow in mass by accreting gas from a reservoir of material in the molecular cloud that may not be bound to any core. SMA1 and SMA4 would be the primary candidates to form high-mass stars in the future due to their position inside the clump, apparently near the center of the gravitational potential. On the other hand, the assumptions initially made in the turbulent core accretion model may not be applicable and may need to be reconsidered to better represent the observations.

However, so far in the discussion, magnetic fields have been ignored and they can add additional support against collapse. Recently, Zhang et al. (2014) obtained dust polarization information toward a sample of 14 massive star-forming regions. They found that magnetic fields in dense cores tend to follow the field orientation in their parental clumps. Therefore, they suggest that the magnetic field plays an important role in the fragmentation of clumps and the formation of dense cores. If magnetic fields are included in the virial equation, the following expression holds:

$$M_{B,\mathrm{vir}} = 3\,\frac{R}{G}\left(\frac{5-2n}{3-n}\right)\left(\sigma^2 + \frac{1}{6}\sigma_{\mathrm{A}}^2\right), \tag{14}$$

where σ_{A} is the Alfvén velocity, and n depends on the density profile (as in Equation (12)). The Alfvén velocity can be determined from

$$\sigma_{\mathrm{A}} = \frac{B}{\sqrt{4\pi\rho}}, \tag{15}$$

where B is the magnitude of the magnetic field and ρ is the mass density of each core, $\rho = \mu_{\mathrm{H_2}}\, m_{\mathrm{H}}\, n(\mathrm{H_2})$.

To maintain virial equilibrium including magnetic fields ($M_{B,\mathrm{vir}}/M_{\mathrm{core}} = 1$), field strengths of 1.7, 1.6, 0.56, and 1.2 mG are needed toward the dust cores embedded in MM1 (SMA1, SMA3, SMA4, and SMA5, respectively). If a uniform density is assumed, $n = 0$ instead of $n = 1.8$, the magnetic field magnitudes are ∼25% lower. On average, magnetic fields of ∼1–2 mG would be needed to maintain the SMA cores in virial equilibrium. Magnetic fields of these strengths are apparently consistent with observations of more evolved high-mass cores. Crutcher et al. (2010) suggest that at densities of $\sim 10^6\,\mathrm{cm^{-3}}$ the most probable maximum strength for the magnetic field is ∼1 mG. Girart et al. (2013) indeed measure the magnitude of the magnetic field toward the high-mass star-forming core DR 21(OH) and determine a value of 2.1 mG at a density of $10^7\,\mathrm{cm^{-3}}$. Although it seems possible to obtain magnetic field magnitudes of ∼1 mG in high-mass star-forming cores (e.g., Qiu et al. 2014; Li et al. 2015), so far, all estimation of field strengths are in cores with current evidence of star formation. No measurements have been made in prestellar sources. Therefore, although the non-magnetized version of the turbulent core accretion model is not consistent with the observed properties of the SMA cores in IRDC G028.23-00.19, which are candidates to form high-mass stars, the magnetized picture still needs to be tested.

If observations indeed prove that the magnetized picture is feasible, it would imply that: (i) star formation efficiencies much larger than 30% would be needed to form high-mass stars in IRDC G028.23-00.19 (30% is the current value most favored by observations, but higher values have been suggested from simulations; e.g., Matzner & McKee 2000) or (ii) IRDC G028.23-00.19 may never form high-mass stars, which would create a new puzzle and it would be necessary to understand why.

The largest possible mass that can be supported by a magnetic field is given by (Bertoldi & McKee 1992)

$$M_B = 16.2\left(\frac{R_e}{Z_e}\right)^2\left(\frac{n(\mathrm{H_2})}{10^6\,\mathrm{cm^{-3}}}\right)^{-2}\left(\frac{B}{\mathrm{mG}}\right)^3 M_\odot, \tag{16}$$

where $2Z_{\mathrm{e}}$ is the length of the symmetry axis and R_e is the radius normal to the axis of an ellipsoidal core. Assuming a spherical core ($Z_e = R_e$) and M_B equal to the mass of SMA1 ($15\,M_\odot$), we find the minimum magnetic field (1.5 mG) that would suppress fragmentation. This magnetic field strength is practically the same as the field strength necessary to maintain the SMA1 core in virial equilibrium (as is also the case for the other cores embedded in the clump MM1). If lower magnetic field strengths are eventually measured, the cores may be prone to fragment.

7. Conclusions

We have imaged the IRDC G028.23-00.19 with the SMA (∼3.″5 at 224 GHz) and JVLA (∼2.″1 at 23 GHz). This IRDC hosts a massive ($1500\,M_\odot$), cold (12 K), and IR dark (at *Spitzer* 3.6, 4.5, 8.0, and 24 μm and at *Herschel* 70 μm) clump, which is one of the most massive, quiescent clumps known (MM1). After examining the dust continuum and the spectral line emission, we draw the following conclusions.

1. Using the SMA dust continuum emission, five dense cores are detected: four of them are embedded in MM1 (SMA1, SMA3, SMA4, and SMA5) and one is located in the northern part of the IRDC (SMA2). There are no cores with a mass larger than $15\,M_\odot$. The lack of high-mass prestellar cores is in disagreement with the turbulent

core accretion model. In order to form a high-mass star, the SMA1 core needs, at least, to double its mass at the same time the central star accretes material. The idea that high-mass stars can form without passing through a high-mass stage in the prestellar phase is consistent with competitive accretion scenarios (e.g., Bonnell et al. 2004; Wang et al. 2010; Myers 2011, 2014).

2. The Jeans mass ($2.2\,M_{\odot}$) is 4–7 times smaller than the core's masses. This is in disagreement with the prediction of competitive accretions models where the clumps fragment in objects with masses similar to the Jeans mass, unless the SMA cores have had sufficient time to accrete and significantly increase their mass.
3. Neither CO wing emission or SiO emission was detected indicating molecular outflows. Thus, confirming that, at the sensitivity of these observations, the SMA cores are starless. To our knowledge, IRDC G028.23-00.19 MM1 is the most massive, cold clump that after interferometric observations maintains the status of "prestellar candidate."
4. At core scales, the NH_3 line widths have some contribution from turbulence, with Mach numbers ranging from 1.1 to 1.8. The gas in the SMA cores is not highly supersonic as the turbulent core accretion suggests.
5. By comparing the thermal and turbulent Jeans masses with the SMA core's masses, we find that the global fragmentation of the clump MM1 is dominated by neither thermal nor turbulent pressure.
6. Unless magnetic fields strengths are about 1–2 mG, the cores are strongly subvirialized ($\alpha < 0.5$). The SMA cores are significantly below equilibrium and likely under fast collapse, which is consistent with cores that can grow in mass.
7. We finally conclude that in IRDC G028.23-00.19 we are witnessing the initial fragmentation of a massive, prestellar clump that will form high-mass stars. Whether the properties observed in IRDC G028.23-00.19 are unique or typical of the very early stages of high-mass star formation needs to be confirmed with a larger well-defined sample.

P.S. gratefully acknowledges Jonathan B. Foster, Satoshi Ohashi, and Fumitaka Nakamura for helpful discussions. P.S. is grateful for the comments from the anonymous referee. A.E. G. thanks FONDECYT No. 3150570. K.W. is supported by grant WA3628-1/1 of the German Research Foundation (DFG) through the priority program 1573 ("Physics of the Interstellar Medium"). Data analysis was in part carried out on the open use data analysis computer system at the Astronomy Data Center (ADC) of the National Astronomical Observatory of Japan.

Facilities: SMA, JVLA.

Software: IDL, MIR, CASA.

Appendix
Derivation of the Maximum Stellar Mass Using the IMF

Adopting the IMF from Kroupa (2001), we have $\xi(m) \propto m^{-1.3}$ for $0.08\,M_{\odot} \leqslant m < 0.5\,M_{\odot}$ and $\xi(m) \propto m^{-2.3}$ for $m \geqslant 0.5\,M_{\odot}$, where m corresponds to the star's mass and $\xi(m)\,dm$ is the number of stars in the mass interval m to $m + dm$. Assuming a range of stellar masses between 0.08 and $150\,M_{\odot}$, we can impose the total number of stars with $m \geqslant m_{\rm max}$ to be unity (in order to assure the formation of one high-mass star, the lowest value for $m_{\rm max}$ should be $8\,M_{\odot}$):

$$1 = \int_{m_{\rm max}}^{150} \xi(m)\,dm. \tag{17}$$

The total mass in a stellar cluster, $M_{\rm cluster}$, is given by

$$M_{\rm cluster} = \int_{0.08}^{150} \xi(m) m\,dm. \tag{18}$$

Combining Equations (17) and (18),

$$M_{\rm cluster} = \frac{\int_{0.08}^{150} \xi(m) m\,dm}{\int_{m_{\rm max}}^{150} \xi(m)\,dm}, \tag{19}$$

and assuming a star formation efficiency, $\epsilon_{\rm sfe}$, of 30% ($M_{\rm cluster} = 0.3 \times M_{\rm clump}$), we can relate $m_{\rm max}$ with the clump mass as

$$m_{\rm max} = \left(\frac{0.3}{\epsilon_{\rm sfe}}\frac{17.3}{M_{\rm clump}} + 1.5 \times 10^{-3}\right)^{-0.77}. \tag{20}$$

To estimate the necessary mass in a clump to form a high-mass star, we can use the following relationship:

$$M_{\rm clump} = \frac{0.3}{\epsilon_{\rm sfe}}\frac{17.3}{(m_{\rm max}^{-1.3} - 1.5 \times 10^{-3})}. \tag{21}$$

and making $m_{\rm max} = 8\,M_{\odot}$, we obtain $260\,M_{\odot}$.

References

Alves, J., Lombardi, M., & Lada, C. J. 2007, A&A, 462, L17
Avison, A., Peretto, N., Fuller, G. A., et al. 2015, A&A, 577, A30
Battersby, C., Bally, J., Jackson, J. M., et al. 2010, ApJ, 721, 222
Beltrán, M. T., Cesaroni, R., Neri, R., et al. 2005, A&A, 435, 901
Benjamin, R. A., Churchwell, E., Babler, B. L., et al. 2003, PASP, 115, 953
Bertoldi, F., & McKee, C. F. 1992, ApJ, 395, 140
Beuther, H., Linz, H., Tackenberg, J., et al. 2013, A&A, 553, A115
Bondi, H. 1952, MNRAS, 112, 195
Bonnell, I. A., & Bate, M. R. 2006, MNRAS, 370, 488
Bonnell, I. A., Bate, M. R., Clarke, C. J., & Pringle, J. E. 2001, MNRAS, 323, 785
Bonnell, I. A., Bate, M. R., & Vine, S. G. 2003, MNRAS, 343, 413
Bonnell, I. A., Vine, S. G., & Bate, M. R. 2004, MNRAS, 349, 735
Bontemps, S., Motte, F., Csengeri, T., & Schneider, N. 2010, A&A, 524, A18
Carey, S. J., Noriega-Crespo, A., Mizuno, D. R., et al. 2009, PASP, 121, 76
Chambers, E. T., Jackson, J. M., Rathborne, J. M., & Simon, R. 2009, ApJS, 181, 360
Chini, R., Hoffmeister, V. H., Nasseri, A., Stahl, O., & Zinnecker, H. 2012, MNRAS, 424, 1925
Clemens, D. P. 1985, ApJ, 295, 422
Commerçon, B., Hennebelle, P., & Henning, T. 2011, ApJL, 742, L9
Contreras, Y., Garay, G., Rathborne, J. M., & Sanhueza, P. 2016, MNRAS, 456, 2041
Contreras, Y., Rathborne, J. M., Guzman, A., et al. 2017, MNRAS, 466, 340
Crutcher, R. M., Wandelt, B., Heiles, C., Falgarone, E., & Troland, T. H. 2010, ApJ, 725, 466
Cyganowski, C. J., Brogan, C. L., Hunter, T. R., et al. 2014, ApJL, 796, L2
Cyganowski, C. J., Brogan, C. L., Hunter, T. R., et al. 2017, MNRAS, 468, 3694
Devereux, N. A., & Young, J. S. 1990, ApJ, 359, 42
Dirienzo, W. J., Brogan, C., Indebetouw, R., et al. 2015, AJ, 150, 159
Duarte-Cabral, A., Bontemps, S., Motte, F., et al. 2013, A&A, 558, A125
Egan, M. P., Shipman, R. F., Price, S. D., et al. 1998, ApJL, 494, L199
Feng, S., Beuther, H., Zhang, Q., et al. 2016a, A&A, 592, A21
Feng, S., Beuther, H., Zhang, Q., et al. 2016b, ApJ, 828, 100
Foster, J. B., Arce, H. G., Kassis, M., et al. 2014, ApJ, 791, 108
Foster, J. B., Jackson, J. M., Barnes, P. J., et al. 2011, ApJS, 197, 25
Garay, G., Mardones, D., Brooks, K. J., Videla, L., & Contreras, Y. 2007, ApJ, 666, 309

Girart, J. M., Beltrán, M. T., Zhang, Q., Rao, R., & Estalella, R. 2009, Sci, 324, 1408
Girart, J. M., Frau, P., Zhang, Q., et al. 2013, ApJ, 772, 69
Guzmán, A. E., Sanhueza, P., Contreras, Y., et al. 2015, ApJ, 815, 130
He, Y.-X., Zhou, J.-J., Esimbek, J., et al. 2015, MNRAS, 450, 1926
Henshaw, J. D., Caselli, P., Fontani, F., et al. 2016, MNRAS, 463, 146
Henshaw, J. D., Caselli, P., Fontani, F., Jiménez-Serra, I., & Tan, J. C. 2014, MNRAS, 440, 2860
Ho, P. T. P., & Townes, C. H. 1983, ARA&A, 21, 239
Hoq, S., Clemens, D. P., Guzmán, A. E., & Cashman, L. R. 2017, ApJ, 836, 199
Hoq, S., Jackson, J. M., Foster, J. B., et al. 2013, ApJ, 777, 157
Jackson, J. M., Rathborne, J. M., Foster, J. B., et al. 2013, PASA, 30, e057
Kauffmann, J., Bertoldi, F., Bourke, T. L., Evans, N. J., II, & Lee, C. W. 2008, A&A, 487, 993
Kauffmann, J., & Pillai, T. 2010, ApJL, 723, L7
Kauffmann, J., Pillai, T., & Goldsmith, P. F. 2013, ApJ, 779, 185
Kim, G., Lee, C. W., Kim, J., et al. 2010, JKAS, 43, 9
Kong, S., Tan, J. C., Caselli, P., et al. 2016, ApJ, 821, 94
Kouwenhoven, M. B. N., Brown, A. G. A., Zinnecker, H., Kaper, L., & Portegies Zwart, S. F. 2005, A&A, 430, 137
Kroupa, P. 2001, MNRAS, 322, 231
Krumholz, M. R., Klein, R. I., & McKee, C. F. 2007a, ApJ, 665, 478
Krumholz, M. R., Klein, R. I., & McKee, C. F. 2007b, ApJ, 656, 959
Krumholz, M. R., & McKee, C. F. 2008, Natur, 451, 1082
Krumholz, M. R., McKee, C. F., & Klein, R. I. 2005, Natur, 438, 332
Krumholz, M. R., McKee, C. F., & Klein, R. I. 2006, ApJ, 638, 369
Lada, C. J., & Lada, E. A. 2003, ARA&A, 41, 57
Larson, R. B. 2003, in Galactic Star Formation Across the Stellar Mass Spectrum, Vol. 287, ed. J. M. De Buizer & N. S. van der Bliek (San Francisco, CA: ASP), 65
Li, H.-B., Yuen, K. H., Otto, F., et al. 2015, Natur, 520, 518
Liu, X.-L., Wang, J.-J., & Xu, J.-L. 2014, MNRAS, 443, 2264
Longmore, S. N., Pillai, T., Keto, E., Zhang, Q., & Qiu, K. 2011, ApJ, 726, 97
López-Sepulcre, A., Cesaroni, R., & Walmsley, C. M. 2010, A&A, 517, A66
Lu, X., Zhang, Q., Wang, K., & Gu, Q. 2015, ApJ, 805, 171
MacLaren, I., Richardson, K. M., & Wolfendale, A. W. 1988, ApJ, 333, 821
Matzner, C. D., & McKee, C. F. 2000, ApJ, 545, 364
McKee, C. F., & Tan, J. C. 2003, ApJ, 585, 850
Miettinen, O. 2014, A&A, 562, A3
Molinari, S., Swinyard, B., Bally, J., et al. 2010, A&A, 518, L100
Mueller, K. E., Shirley, Y. L., Evans, N. J., II, & Jacobson, H. R. 2002, ApJS, 143, 469
Myers, A. T., McKee, C. F., Cunningham, A. J., Klein, R. I., & Krumholz, M. R. 2013, ApJ, 766, 97
Myers, P. C. 2011, ApJ, 743, 98
Myers, P. C. 2014, ApJ, 781, 33
Ohashi, S., Sanhueza, P., Chen, H.-R. V., et al. 2016, ApJ, 833, 209
Ossenkopf, V., & Henning, T. 1994, A&A, 291, 943
Perault, M., Omont, A., Simon, G., et al. 1996, A&A, 315, L165
Peretto, N., & Fuller, G. A. 2009, A&A, 505, 405
Pillai, T., Kauffmann, J., Wyrowski, F., et al. 2011, A&A, 530, A118
Pillai, T., Wyrowski, F., Menten, K. M., & Krügel, E. 2006, A&A, 447, 929
Qiu, K., Zhang, Q., Menten, K. M., et al. 2014, ApJL, 794, L18
Ragan, S. E., Henning, T., Beuther, H., Linz, H., & Zahorecz, S. 2015, A&A, 573, A119
Rathborne, J. M., Jackson, J. M., Chambers, E. T., et al. 2010, ApJ, 715, 310
Rathborne, J. M., Jackson, J. M., Zhang, Q., & Simon, R. 2008, ApJ, 689, 1141
Rathborne, J. M., Whitaker, J. S., Jackson, J. M., et al. 2016, PASA, 33, e030
Reid, M. J., Menten, K. M., Zheng, X. W., et al. 2009, ApJ, 700, 137
Rosero, V., Hofner, P., Claussen, M., et al. 2016, ApJS, 227, 25
Rosero, V., Hofner, P., McCoy, M., et al. 2014, ApJ, 796, 130
Rydbeck, O. E. H., Sume, A., Hjalmarson, A., et al. 1977, ApJL, 215, L35
Sakai, T., Sakai, N., Foster, J. B., et al. 2013, ApJL, 775, L31
Sakai, T., Sakai, N., Furuya, K., et al. 2012, ApJ, 747, 140
Sakai, T., Sakai, N., Furuya, K., et al. 2015, ApJ, 803, 70
Sakai, T., Sakai, N., Kamegai, K., et al. 2008, ApJ, 678, 1049
Sanhueza, P., Garay, G., Bronfman, L., et al. 2010, ApJ, 715, 18
Sanhueza, P., Jackson, J. M., Foster, J. B., et al. 2012, ApJ, 756, 60
Sanhueza, P., Jackson, J. M., Foster, J. B., et al. 2013, ApJ, 773, 123
Shipman, R. F., van der Tak, F. F. S., Wyrowski, F., Herpin, F., & Frieswijk, W. 2014, A&A, 570, A51
Shirley, Y. L., Ellsworth-Bowers, T. P., Svoboda, B., et al. 2013, ApJS, 209, 2
Shirley, Y. L., Huard, T. L., Pontoppidan, K. M., et al. 2011, ApJ, 728, 143
Shu, F. H. 1977, ApJ, 214, 488
Simon, R., Jackson, J. M., Rathborne, J. M., & Chambers, E. T. 2006, ApJ, 639, 227
Smith, R. J., Longmore, S., & Bonnell, I. 2009, MNRAS, 400, 1775
Tan, J. C., Beltrán, M. T., Caselli, P., et al. 2014, Protostars and Planets VI, 149
Tan, J. C., Kong, S., Butler, M. J., Caselli, P., & Fontani, F. 2013, ApJ, 779, 96
Tan, J. C., Kong, S., Zhang, Y., et al. 2016, ApJL, 821, L3
Traficante, A., Fuller, G. A., Peretto, N., Pineda, J. E., & Molinari, S. 2015, MNRAS, 451, 3089
Urquhart, J. S., Moore, T. J. T., Csengeri, T., et al. 2014, MNRAS, 443, 1555
Vasyunina, T., Vasyunin, A. I., Herbst, E., et al. 2014, ApJ, 780, 85
Vuong, M. H., Montmerle, T., Grosso, N., et al. 2003, A&A, 408, 581
Wang, K., Zhang, Q., Testi, L., et al. 2014, MNRAS, 439, 3275
Wang, K., Zhang, Q., Wu, Y., Li, H.-b., & Zhang, H. 2012, ApJL, 745, L30
Wang, K., Zhang, Q., Wu, Y., & Zhang, H. 2011, ApJ, 735, 64
Wang, P., Li, Z.-Y., Abel, T., & Nakamura, F. 2010, ApJ, 709, 27
Wang, Y., Zhang, Q., Rathborne, J. M., Jackson, J., & Wu, Y. 2006, ApJL, 651, L125
Yanagida, T., Sakai, T., Hirota, T., et al. 2014, ApJL, 794, L10
Zhang, Q., Qiu, K., Girart, J. M., et al. 2014, ApJ, 792, 116
Zhang, Q., Wang, K., Lu, X., & Jiménez-Serra, I. 2015, ApJ, 804, 141
Zhang, Q., Wang, Y., Pillai, T., & Rathborne, J. 2009, ApJ, 696, 268